Mon. Not. R. Astron. Soc. (2011) doi:10.1111/j.1365-2966.2011.20188.x

Stellar population gradients in the cores of nearby field E+A galaxies

Michael B. Pracy,[1,2⋆] Matt S. Owers,[1] Warrick J. Couch,[1] Harald Kuntschner,[3] Kenji Bekki,[4] Frank Briggs,[5] Philip Lah,[5,6] and Martin Zwaan[3]

[1]*Centre for Astrophysics & Supercomputing, Swinburne University of Technology, PO Box 218, Hawthorn, VIC 3122, Australia*
[2]*Sydney Institute for Astronomy, School of Physics, University of Sydney, NSW 2006, Australia*
[3]*European Southern Observatory, Karl-Schwarzschild Strasse 2, 85748 Garching, Germany*
[4]*ICRAR, M468, The University of Western Australia, 35 Stirling Highway, Crawley, Western Australia 6009, Australia*
[5]*Mount Stromlo Observatory, The Australian National University, Weston Creek, ACT 2611, Australia*
[6]*National Centre for Radio Astrophysics, Post Bag 3, Ganeshkhind, Pune 411 007, India*

Accepted 2011 November 11. Received 2011 October 6; in original form 2011 July 18

ABSTRACT

We have selected a sample of local E+A galaxies from the Sloan Digital Sky Survey (SDSS) Data Release 7 for follow-up integral field spectroscopy with the Wide Field Spectrograph (WiFeS) on the Australian National University's (ANU) 2.3-m telescope. The sample was selected using the Hα line in place of the [O II] λ3727 line as the indicator of ongoing star formation (or lack thereof). This allowed us to select a lower redshift sample of galaxies than available in the literature since the [O II] λ3727 falls off the blue end of the wavelength coverage in the SDSS for the very lowest redshift objects. This low-redshift selection means that the galaxies have a large angular to physical scale which allows us to resolve the central $\sim$1 kpc region of the galaxies; the region where stellar population gradients are expected. Such observations have been difficult to make using other higher redshift samples because even at redshifts $z \sim 0.1$ the angular to physical scale is similar to the resolution provided by ground-based seeing. Our integral field spectroscopy has enabled us to make the first robust detections of Balmer line gradients in the centres of E+A galaxies. Six out of our sample of seven, and all the galaxies with regular morphologies, are observed to have compact and centrally concentrated Balmer line absorption. This is evidence for compact young cores and stellar population gradients which are predicted from models of mergers and tidal interactions which funnel gas into the galaxy core. Given the generally isolated nature of our sample, this argues for the galaxies being seen in the late stage of a merger where the progenitors have already coalesced.

Key words: galaxies: evolution – galaxies: formation – galaxies: stellar content.

1 INTRODUCTION

E+A galaxies, their optical spectra characterized by strong Balmer absorption lines and little or no emission, represent galaxies undergoing rapid evolution in their star formation properties. The strong Balmer lines are indicative of a substantial population of A-type stars which must have formed within the last $\sim$1 Gyr. However, the lack of optical emission lines implies that the episode of star formation in which they formed has ended and star formation is not ongoing. The normal interpretation of this spectral signature is that the galaxy is being observed in a post-starburst phase (e.g. Couch & Sharples 1987; Poggianti et al. 1999), although it can also be produced by the abrupt truncation of star formation in a disc, without necessarily requiring a starburst (e.g. Shioya, Bekki & Couch 2004; Bekki et al. 2005; Pracy et al. 2005). This spectroscopic evolution may be accompanied by a morphological one where a star-forming disc galaxy is transformed into a quiescent spheroidal system (Caldwell et al. 1996; Zabludoff et al. 1996).

Much attention has been paid to the environmental influences which give rise to the abrupt changes in star formation rate within E+A galaxies and several processes have been suggested. These include major and unequal mass galaxy mergers (Mihos & Hernquist 1996; Bekki et al. 2005), galaxy–galaxy interactions with mass ratios close to unity (Bekki et al. 2005) and, in the cluster environment, interactions with the cluster tidal field (Bekki, Shioya & Couch 2001), galaxy harassment (Moore, Lake & Katz 1998) and interaction with the intracluster medium (Gunn & Gott 1972; Dressler & Gunn 1983; Bothun & Dressler 1986). While the situation in galaxy clusters remains somewhat unclear (Pracy, Couch & Kuntschner 2010), there is growing consensus that galaxy mergers are the mechanism responsible for producing the local field

⋆E-mail: mpracy@physics.usyd.edu.au

E+A population as seen in the analysis of E+A samples from large redshift surveys. Ground-based imaging and *Hubble Space Telescope* follow-up of a sample of 21 E+A galaxies selected from the Las Campanas Redshift Survey (LCRS) revealed an increased rate of tidal features implying galaxy mergers had taken place (Zabludoff et al. 1996; Yang et al. 2008). Using a sample selected from the Two Degree Field Galaxy Redshift Survey (2dFGRS), Blake et al. (2004) concluded that the significant incidence of tidal disruption, the nature of the luminosity function, and the results of a near-neighbour analysis were consistent with them being in the late stage of a merger. Goto (2005) found a higher incidence of near neighbours for E+A galaxies in the Sloan Digital Sky Survey (SDSS) suggesting galaxy–galaxy interactions may also be an important mechanism.

Another, more direct, way of discerning the physical cause of the E+A phase is to examine the internal properties of the galaxy itself. The internal kinematics and spatial distribution of the young and old stellar populations are expected to differ between different formation scenarios. For example, in a major merger the young stellar population should quickly become dynamically pressure supported (Norton et al. 2001; Bekki et al. 2005). For more extreme mass ratio mergers and tidal interactions, significant rotation of the young stellar population is generally expected (Bekki et al. 2005). The two major spatially resolved spectroscopic studies of low-redshift 'field' E+A galaxies (Norton et al. 2001; Pracy et al. 2009) have reached quite different conclusions on the prevalence of rotation in E+A galaxies. Using follow-up slit spectroscopy of the LCRS sample, Norton et al. (2001) found little evidence for rotation in most cases. In contrast, the Pracy et al. (2009) two-dimensional Integral Field Unit (IFU) spectroscopy of a subsample of the Blake et al. (2004) 2dFGRS E+A galaxies showed rotation of the young stellar population to be ubiquitous. This discrepancy could partly be explained by the rotation axis not always corresponding to the isophotal major axis, dampening the amount of rotation measured using a one-dimensional slit (Pracy et al. 2009).

If the E+A phase is the result of gas-rich mergers, then evidence of this should be contained in the spatial distribution of the stellar populations. During a merger, tidal torques transfer angular momentum from the gas to the stars (Barnes & Hernquist 1996), driving the gas towards the centre and resulting in a compact central starburst (Mihos & Hernquist 1994, 1996; Barnes & Hernquist 1996; Hopkins et al. 2009). Feedback processes then halt the starburst (Springel & Hernquist 2003; Springel, Di Matteo & Hernquist 2005) leaving an old stellar population that is distributed like a normal early-type galaxy (e.g. Hernquist 1992; Hopkins et al. 2009) and a young component that forms a centrally concentrated cusp (Mihos & Hernquist 1994; Hopkins et al. 2009). This young component should be quite compact, with scales of $\lesssim$1 kpc (Barnes & Hernquist 1996; Bekki et al. 2005; Hopkins et al. 2009), and is a possible explanation of the excess light observed in the centres of merging starburst galaxies (Hibbard & Yun 1999; Rothberg & Joseph 2004). Kohno et al. (2002) detected centrally concentrated diffuse and gravitationally stable molecular gas in the post-starburst galaxy NGC 5195 which may be the remaining component of the gas used in fuelling the central starburst. In the E+A galaxies the remnant of such a starburst should be observable as a Balmer line absorption enhancement and gradient within the central $\sim$1 kpc (Bekki et al. 2005; Pracy et al. 2005). These predictions of mergers resulting in a centrally concentrated post-starburst region and strong radial gradients have been strengthened by a recent set of detailed fully three-dimensional hydrodynamic simulations of E+A galaxy production from galaxy merging taking into account a wide range of initial parameters such as mass, gas fraction, orbital configuration, mass ratio and dust properties (Snyder et al. 2011).

Attempts to measure the spatial distribution of the post-starburst stellar population in E+A galaxies have been hindered by the small expected angular scale of the starburst remnant at the redshifts of E+A galaxies selected from large redshift surveys (Blake et al. 2004; Goto 2007), where it is smaller or comparable to the typical seeing scale. For example, at the median redshift of these surveys ($z \sim 0.1$), the 1 kpc expected scale of the starburst projects to $\sim$0.5 arcsec. Norton et al. (2001) compared the radial distribution of the young and old populations in the LCRS sample and concluded that the young stellar population was centrally concentrated. The seeing full width at half-maximum (FWHM) of the Norton et al. (2001) observations corresponded to $\sim$2–3 kpc, and in about half the cases they were able to spatially resolve the young stellar population by showing it to be broader than the stellar point spread function. The implication, in these cases at least, was that the starburst population is not confined to the galaxy core ($\sim$1 kpc). Likewise, follow-up of a H I-detected post-starburst galaxy from the SDSS by Chilingarian, De Rijcke & Buyle (2009) found the very young stellar population spread over the central $\sim$2.5 kpc. Yagi & Goto (2006) analysed three early-type E+A galaxies selected from the SDSS using long-slit spectroscopy. In one galaxy they could successfully estimate a Hδ equivalent width (EW) profile; they found that the post-starburst signature was as extended as the continuum light, and in the other two galaxies concluded (on statistical grounds) that the post-starburst region was also significantly extended. Pracy et al. (2009) were unable to detect any Balmer line gradients in their sample although their limited spatial coverage coupled with spatial resolution constraints imposed by the delivered image quality meant they could not robustly rule out compact gradients in the stellar populations.

In this paper we circumvent these physical-scale resolution issues by investigating a new, very low-redshift sample of E+A galaxies which have large angular to physical size scales. This is achieved by modifying the standard definition of an E+A galaxy, using the Hα line as the constraint on emission (and hence ongoing star formation) instead of the traditional [O II] λ3727 line. This change allows selection of a local sample of E+A galaxies at $z < 0.01$ to easily resolve their central 1 kpc.

In what follows, Section 2 describes the details of the sample selection; Section 3 describes the observations, data reduction and analysis; in Section 4 we present our results, including spatially resolved Balmer line maps; and in Section 5 we discuss these results. Our conclusions are given in Section 6. Throughout, we adopt an $\Omega_{\rm M} = 0.3$, $\Omega_{\Lambda} = 0.7$ and $H_0 = 70\,{\rm km\,s^{-1}\,Mpc^{-1}}$ cosmology.

2 THE SAMPLE

2.1 Selection criteria

E+A galaxies are rare in the local Universe (Zabludoff et al. 1996; Blake et al. 2004; Goto 2007) and there are very few nearby ($z < 0.01$) examples known. For example, from the 2dFGRS, Blake et al. (2004) catalogued 56 E+A galaxies but only two of these had redshifts of $z < 0.01$. The catalogue of E+A galaxies produced from the much larger SDSS by Goto (2007) has no E+A galaxies with redshifts of $z < 0.03$. The dearth of E+A galaxies is the result of the spectral range of the SDSS spectra ($\lambda \gtrsim 3800$ Å) not containing the [O II] λ3727 line for the very lowest redshift objects and not a result of a true lack of local E+A galaxies in the SDSS. Although the E+A fraction does increase rapidly with redshift (e.g. Poggianti

et al. 1999; Snyder et al. 2011). The use of low or non-existent EWs of the [O II] λ3727 line as the constraint on ongoing star formation is historical, since E+A galaxies were originally discovered and studied in intermediate-redshift clusters (Dressler & Gunn 1983) where the Hα line was not available. In fact, at low redshift the Hα line is a more natural choice for this, since it is more easily relatable to the star formation rate, intrinsically stronger, less prone to dust obscuration and has been shown to be a more robust constraint on star formation in E+A galaxies (Blake et al. 2004). By replacing the [O II] λ3727 constraint with the one defined using the Hα line, we have selected a $z < 0.01$ E+A sample from the SDSS Data Release 7 spectral line catalogue. The selection criteria used were (our definition of EW has emission denoted as negative values) the following.

(i) Little or no Hα emission: EW(Hα) > -2.5 Å.
(ii) Strong absorption in the Hδ line: EW(Hδ) > 5.0 Å.
(iii) We also demand strong absorption in the Hγ and Hβ lines since this has been shown to select a much higher fidelity sample (Blake et al. 2004): EW(Hγ) and EW(Hβ) > 4.0 Å.
(iv) Small errors on the EW measurements of the Balmer absorption lines: the errors in each of EW(Hδ), EW(Hγ), EW(Hβ) $<$ 1.0 Å.
(v) High-quality redshift: probability the redshift is correct $z_{\rm confidence} > 0.95$.
(vi) Low redshift: $0.0005 < z < 0.01$.
(vii) Sufficiently bright for IFU follow-up: $r < 15.5$ mag.

In addition to these criteria, there were also constraints on the right ascension and declination for follow-up observations. In total, this gave us eight possible targets that could be observed during our scheduled telescope time and we obtained data for all but one. In the absence of right ascension and declination constraints, 20 galaxies in the SDSS meet these criteria. Imposing constraints on the Hβ and Hγ lines in addition to Hδ has a significant effect on the sample size, particularly Hβ which is prone to emission line filling. Removing the Hβ constraint increases the sample size from 20 to 30, whilst removing the Hγ constraint increases the sample by a single object; removing both constraints results in a sample of 37 galaxies. The final observed targets and their properties are given in Table 1.

A consequence of selecting an E+A galaxy sample from the local volume is that our sample contains intrinsically fainter galaxies than those selected at higher redshift. Fig. 1 shows our sample in a M_R versus $g-r$ colour magnitude diagram (blue diamonds) along with the Pracy et al. (2009) sample (red triangles). The brightest galaxy in this sample corresponds to the faint end of the Pracy et al. (2009) sample in magnitude and colour. There is a strong correlation in the local sample between colour and luminosity in the sense that the fainter galaxies are bluer.

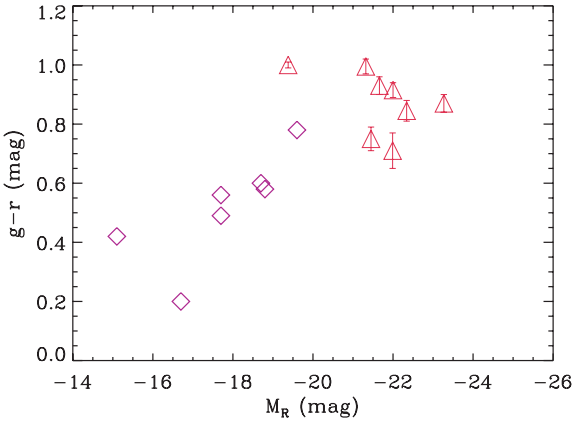

Figure 1. Colour versus absolute magnitude for our current sample (blue diamonds) and the Pracy et al. (2009) sample (red triangles) at redshifts between 0.04 and 0.20. The error bars on the Pracy et al. (2009) points give an indication of the uncertainty in the *k*-corrections.

2.2 SDSS data

The SDSS spectra of our sample are shown in Fig. 2. Three galaxies have detectable Hα emission (E+A 2, E+A 3 and E+A 5). Two of these galaxies have [N II] λ6583/Hα λ6563 > 1 with the other having [N II] λ6583/Hα λ6563 ~ 1. Such ratios are generally indicative of active galactic nucleus (AGN) activity (Baldwin, Phillips & Terlevich 1981), although in this case we have selected galaxies with weak Hα emission and underlying stellar populations with strong Balmer line absorption. In this circumstance, the underlying absorption can have a large effect on the apparent ratio of the lines, and we show later that these spectra are more consistent with a combination of star formation and AGN activity. The spectra all have strong higher order Balmer lines (as selected) and blue continua – E+A 5 has a significantly redder continuum than the remainder of

Table 1. Target galaxies and their properties.

SDSS object ID	ID	r (mag)	$g-r$	z	M_r (mag)	scale (kpc arcsec^{-1})	Hδ Å	Morphology and environment notes
587725073921278177	E+A 1	14.92	0.20	0.005	−16.7	0.10	−6.1	Irregular morphology with lower mass starbursting companion 5 kpc away.
587726033847451681	E+A 2	12.35	0.58	0.004	−18.8	0.08	−5.2	NGC 3156. Isolated early type. Member of the SAURON sample.
588017724397912097	E+A 3	15.26	0.49	0.009	−17.7	0.18	−5.8	NGC 3976A. Late-type disc located ∼50 kpc from much more massive NGC 3976.
588017730298576932	E+A 4	14.50	0.42	0.002	−15.1	0.04	−5.4	In the Virgo cluster. No evidence of interaction.
588848898841903109	E+A 5	12.80	0.78	0.007	−19.6	0.14	−6.0	NGC 4418. Semi-isolated early type. Starbursting companion ∼17 kpc away.
587729779053887547	E+A 6	12.98	0.60	0.005	−18.7	0.10	−6.3	Isolated early type
587726033341513813	E+A 7	14.67	0.56	0.007	−17.7	0.14	−6.4	Isolated early type

Notes. Basic properties of our sample. Column 1 is the SDSS object ID and Column 2 is our simplified name. The remainder of the columns are SDSS *r*-band magnitude, $g-r$ colour, redshift, absolute *r* magnitude, angular to physical scale, Hδ absorption-line EW from the SDSS integrated spectrum, and a short description of the morphology and local environment from visual inspection of the SDSS imaging for each galaxy and the surrounding region.

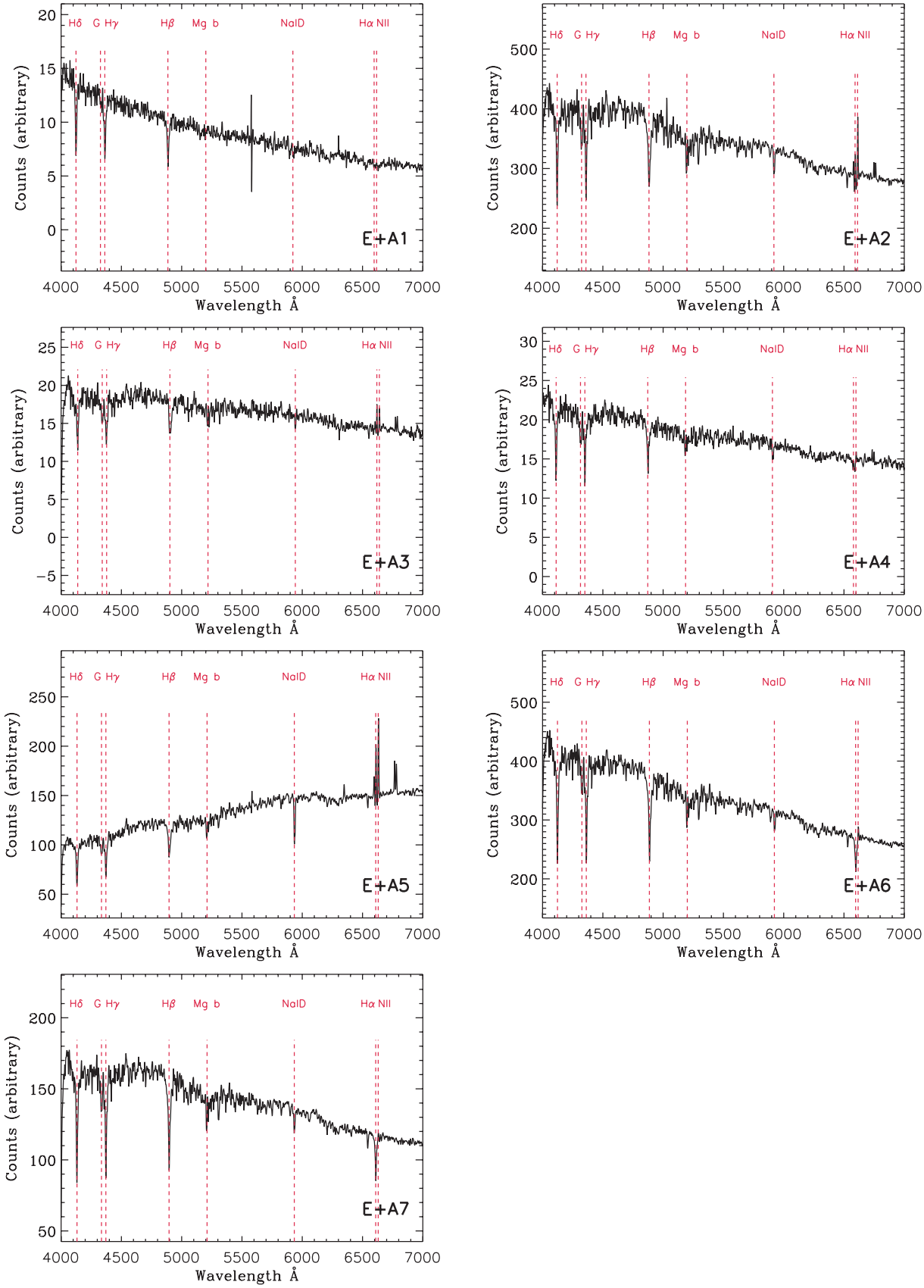

Figure 2. Spectra of our sample of E+A galaxies from the SDSS Data Release 7.

the sample but still has an integrated colour that is quite blue with $g - r = 0.78$.

Colour SDSS images of the sample are shown in the leftmost column of Fig. 3. The galaxies in the sample generally have early-type morphologies, which is typical of E+A samples. There are two exceptions: E+A 1 which has an irregular morphology and is also the bluest (youngest stellar population) galaxy in our sample and E+A 3 which is a late-type disc galaxy.

3 OBSERVATIONS AND DATA REDUCTION

3.1 Observations

Our data were obtained using the Wide Field Spectrograph (WiFeS; Dopita et al. 2007, 2010) on the Mount Stromlo and Siding Springs Observatory's 2.3-m telescope. The WiFeS is an image-slicing integral field spectrograph with a $25 \times 38\,\mathrm{arcsec}^2$ field of view. The spatial pixel size is 1 arcsec^2 (after on-chip binning) and the spectra have a resolution of $R \sim 3000$ and cover from ∼3500 to ∼9000 Å. The WiFeS is designed for nod and shuffle observations and we used the instrument in this mode. This mode of observation would not normally be used for observations concerned primarily with the blue end of the optical spectrum. However, in this case our objects filled the entire field of view so classical sky subtraction was not possible. The nod and shuffle technique was chosen over observations of offset sky fields (which would have been more efficient) to minimize systematics. The WiFeS CCD is read out by four separate amplifiers and as such the four quadrants have different characteristics. We positioned our targets away from the centre of the WiFeS field of view in the bottom-right quadrant (see Fig. 3). This was done to avoid the galaxy centre being located where the four readout sections meet. The observations were obtained over a five night dark-time run in 2010 March. Table 2 summarizes our observations.

3.2 Data reduction

The data were reduced using the WiFeS IRAF data reduction package (Dopita et al. 2010). The raw frames were bias-subtracted using the overscan region and trimmed. Since the data were taken in nod and shuffle mode, sky subtraction is performed by shifting the image so that the sky regions are moved to the corresponding primary region and subtracted from the original image. Flat-fielding was performed utilizing quartz–halogen lamp exposures. At this point the individual slice regions were extracted into separate image extensions. The wavelength solution was derived and applied using CuAr arc lamp exposures. The slices were then combined into a single three-dimensional data cube.

3.3 Adaptive binning

Within each data cube there is a large variation of the spectrum signal-to-noise ratio (S/N) achieved depending on its spatial position. For the most part the S/N ratio drops off rapidly moving away from the bright galaxy centre. In general, the S/N of a 1-arcsec spaxel in the central regions is sufficient for quantitative analysis (S/N ∼ 10 Å^{-1}). However, in the outer regions single 1-arcsec spaxels do not provide sufficient quality spectra. In order to increase the S/N in the outer parts and to obtain more consistent spectral quality across the field of view, we bin the data spatially using the Voronoi spatial binning method of Cappellari & Copin (2003). This method adaptively bins spatial pixels in such a way as to obtain approximately the same S/N in each final spatial bin. This results in smaller spatial bins in the central region and progressively larger bin sizes moving outwards. A different final S/N per adaptive bin was chosen for each galaxy depending on the quality of the data; the final S/N values ranged from ∼6 to 12 Å^{-1} spaxel^{-1}.

3.4 Recession velocities

We measure the recession velocity of each spatially binned spectrum by fitting them with rest-frame template spectra. The template spectra used were from the single-age single-metallicity stellar population models of Vazdekis et al. (2007) which are constructed from empirical stellar spectra (Sánchez-Blázquez et al. 2006). The stellar population ages used in the models ranged from ∼100 Myr to ∼13 Gyr. The spectral resolution of the science data is degraded to match that of the templates. The fitting is then performed using the penalized pixel fitting algorithm of Cappellari & Emsellem (2004) which fits the spectrum using a combination of input template spectra and simultaneously fitting for the recession velocity and velocity dispersion.

3.5 Line indices

We measure line EWs from each spectrum using the flux-summing technique. This uses three wavelength bands to define the EW; one centred on the line itself and two flanking bands on either side of the line to define the expected continuum level by linear extrapolation. For lines at the blue end of the spectrum, including Hδ, Hγ and Hβ, we measure line strength EWs on the Lick/Intermediate Dispersion Spectrograph system (Worthey & Ottaviani 1997; Trager et al. 1998). Prior to measuring the indices, the science spectra are convolved with a wavelength-dependent Gaussian to the Lick resolution (∼9 Å). For lines redwards of the Lick indices, in particular Hα and [N II] λ6583 that do not have standard definitions, we again use the flux-summing technique with appropriate line and continuum bands.

4 RESULTS

4.1 Balmer line gradients

In the third column of Fig. 3 we show the EW maps for the Hδ, Hγ and Hβ lines combined as a straight average. The trends in these maps are also present in each of the individual line maps, but combining the lines results in greater S/N. The EW maps can be compared with the distribution of overall galaxy light shown in column 2 by collapsing the light through the original unbinned IFU elements along the wavelength direction and column 1 which shows an SDSS colour image with the IFU field of view superimposed. *In every case except E+A 1, there is strong enhancement in the Balmer line absorption EW concentrated in the galaxy core on scales <1 kpc*. E+A 1 has a uniform very strong Hδ signature spread across the entire extent of the galaxy. It also differs to the rest of the sample in other respects: it is the only irregular system and easily the bluest galaxy in the sample. As mentioned in Table 1, E+A 2 (NGC 3156) is a member of the Spectroscopic Areal Unit For Research on Optical Nebulae (SAURON) sample (de Zeeuw et al. 2002) enabling us to compare our Balmer absorption line map with the Hβ map of Kuntschner et al. (2010), and we note that the maps are in good agreement. In the last column of Fig. 3 we have

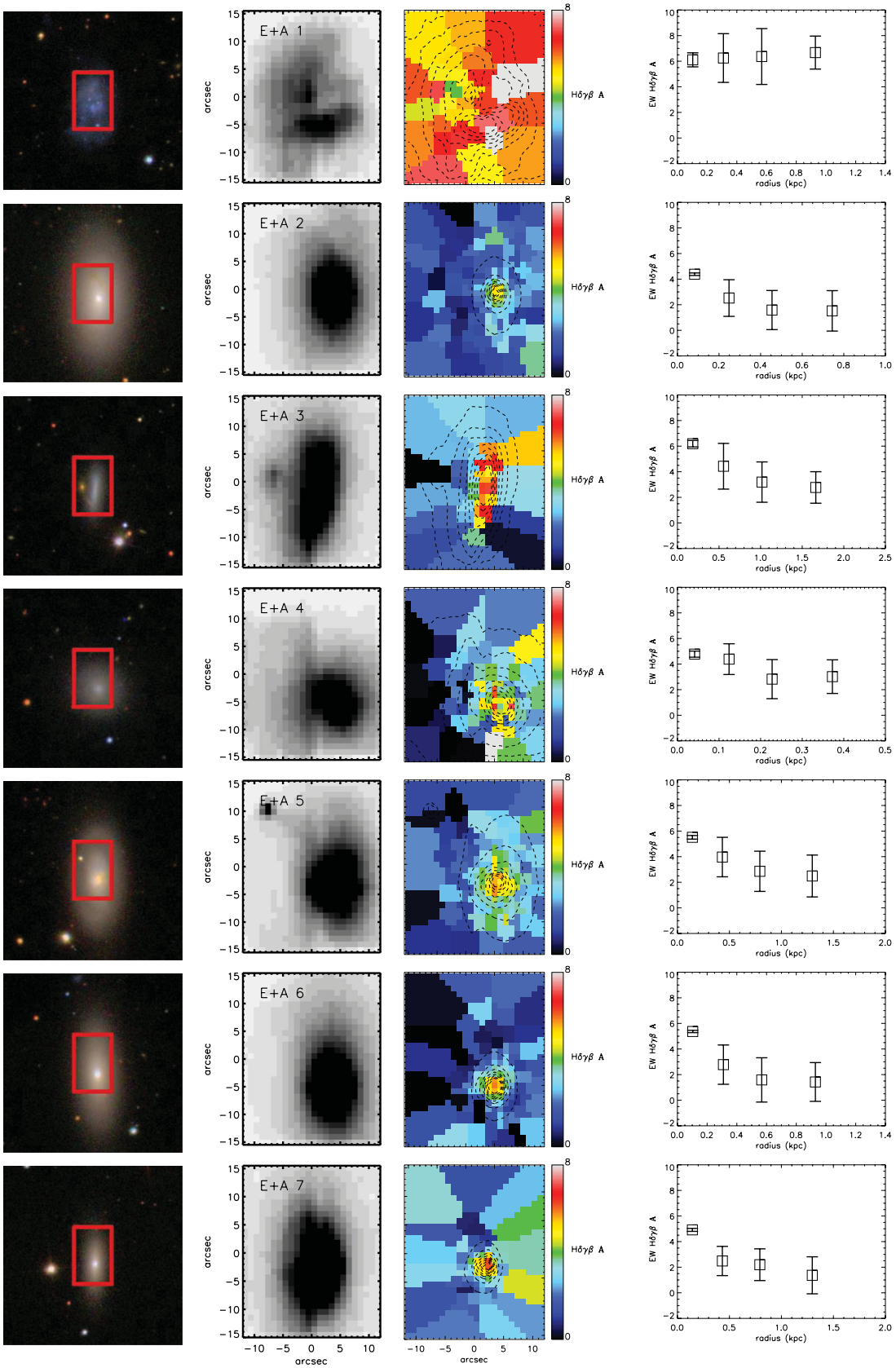

Figure 3. One object per row – from left to right: SDSS image with the size, orientation and position of the WiFeS field of view superimposed; reconstructed image by collapsing the WiFeS data in the spectral direction; Balmer line EW maps for $H\delta + H\gamma + H\beta$. The overlaid contours are the continuum light profiles; radial Balmer line gradients based on azimuthal binning of the WiFeS spectra. Note that the horizontal axis scale in the final column changes.

Table 2. Summary of observations.

ID	Exposure time (s) object; sky	*N* (readouts)	PA	Seeing (arcsec)
E+A 1	2880; 2880	2	155	1.7
E+A 2	1200; 1200	1	50	1.7
E+A 3	8040; 8040	4	140	3.0
E+A 4	6600; 6600	4	180	2.0
E+A 5	3600; 3600	3	60	1.7
E+A 6	1440; 1440	1	170	1.6
E+A 7	3600; 3600	3	175	1.7

Notes. From left to right: object ID; total exposure times on object and on sky; the number of readouts; the position angle of the WiFeS IFU; and an estimate of the seeing during the observation.

azimuthally binned the data before measuring line indices to construct radial Balmer line gradients. The Balmer line enhancement seen in the two-dimensional maps are seen as negative Balmer line radial gradients. These radial profiles of the Balmer line EW are similar to those predicted from merger models; cf. fig. 9 of Pracy et al. (2005). The observed gradients are confined to a smaller radius than the models (which show enhancements with a negative gradient over ∼2 kpc), but this is expected given the models are for significantly brighter galaxies which should have a larger central starburst region.

In Fig. 4 we show an age–metallicity diagnostic diagram for our galaxies using the Hδ and $C_2$4668 lines. The line ratios are shown for the radial data with the smallest *red diamond* representing the innermost radial point and increasing radii represented by increasing larger symbol sizes. The age–metallicity grids are from the single stellar population models of Thomas, Maraston & Bender (2003) and Thomas, Maraston & Korn (2004) and assume solar abundance ratios. The Balmer line radial gradients can be seen as luminosity-weighted age gradients in this plot. In general, the smaller inner radial data points have younger ages than those at larger radii. The inner radial regions have ages $\lesssim$1 Gyr consistent with what is expected for E+A galaxies and similar to the global ages of the Pracy et al. (2009) E+A sample which are overlaid as *green squares*.

4.2 Mass fractions

We estimated the mass in recently formed stars from the best-fitting stellar population templates as described in Section 3.4. In this case, we constructed a spatially integrated spectrum for each of our sample by summing over all spaxels within a circular aperture of radius 11 arcsec. We fitted the spectra with a combination of a single old stellar population of age ∼13 Gyr and a set of young stellar population models with ages ranging from 100 Myr to ∼1 Gyr (all model stellar populations assumed solar metallicity) and calculated the mass fraction of the young stellar population. This results in burst mass fraction estimates of between ∼6 and 12 per cent for all galaxies in our sample except E+A 1 which is best fitted with 100 per cent young mass fraction, i.e. we are unable to quantify the old stellar population in this galaxy. These mass fractions correspond to the young stellar population contributing between 51 and 63 per cent of the light between 4500 and 5500 Å. The calculated burst mass fractions are not sensitive to the precise age chosen for the old stellar population, since the spectra of old stellar populations do not change rapidly with age. For the young population, there are degeneracies between age and burst fraction in the sense that decreasing the age of the stellar population has a similar effect as increasing the burst fraction. To illustrate this, we fitted again allowing the combination of only two models. First we fitted an old ∼13 Gyr model and a young stellar population of age 890 Myr which resulted in the mass fraction estimates increasing to between 11 and 17 per cent (E+A 1 again returns a 100 per cent young mass fraction and is poorly fitted by this combination). We also fitted the combination of a ∼13 Gyr model and a younger 500 Myr template which resulted in the range of mass fractions decreasing to ∼3–4 per cent (E+A 1 has a young mass fraction of ∼25 per cent under these assumptions). These lower burst fractions by mass still contribute significantly to the overall light (between 40 and 50 per cent) since the younger stellar populations have a smaller mass-to-light ratio. Reducing the age of the young fraction reduces the burst mass fractions further but results in progressively poorer fits (again the exception is E+A 1 which is better fitted by a younger population). Overall, the recently formed stars account for of order 10 per cent of the total stellar mass but contribute more than half the total light at ∼5000 Å.

4.3 Aperture effects

The presence of such strong radial gradients in the Balmer lines means the classification of these objects is strongly dependent on aperture effects. The measured EW of the Balmer lines will depend on the physical scale probed which in turn depends on both the distance of the object and the angular size subtended by the fibre. At a given distance, a smaller fibre will measure a larger absorption line strength since the light is dominated by the central region with a large EW, as the fibre size is increased the light becomes more contaminated by the outer regions where the absorption EW is small. Likewise, for a fixed aperture the Balmer line EW measured will decrease with distance as the angular size of the galaxy decreases and more of the outer regions of the galaxy are within the fibre aperture. This means, independent of apparent magnitude constraints, galaxies that fit the EW selection criteria at low redshift may not if they were observed at higher redshift. This is illustrated for our sample in Fig. 5, where we have measured the Hδ EW for different sized apertures. The horizontal axis shows the effective redshift the object would be at to subtend a 3-arcsec aperture (which is the fibre aperture of the SDSS), i.e. we have measured the Hδ EW in our IFU data with an aperture that is the same physical size as a 3-arcsec aperture would be at that redshift. This demonstrates how the Hδ EW measured would decrease for our objects if they were observed at higher redshift. The horizontal *solid black line* indicates the Hδ EW selection limit for our sample. All of our sample (except E+A 1 which does not display a radial gradient) would have Hδ EWs below the selection limit if observed at $z \gtrsim 0.06$.

4.4 Emission lines

As mentioned in Section 2.2, three of the galaxies have integrated spectra that have Hα in emission. This emission is weak, by selection, since we required EW(Hα) > -2.5 Å. In all three cases, the ratio [N II] λ6583/Hα λ6563 $\gtrsim$ 1, which is indicative of AGN activity rather than star formation (e.g. Baldwin et al. 1981; Veilleux & Osterbrock 1987; Kewley et al. 2001). However, as a result of our selection of spectra with both weak or non-existent Hα emission and a stellar continuum with strong Balmer lines in absorption, we therefore expect strong Hα absorption in the stellar continuum underlying the emission line. Hence the [N II] λ6583/Hα λ6563 ratio is significantly overestimated.

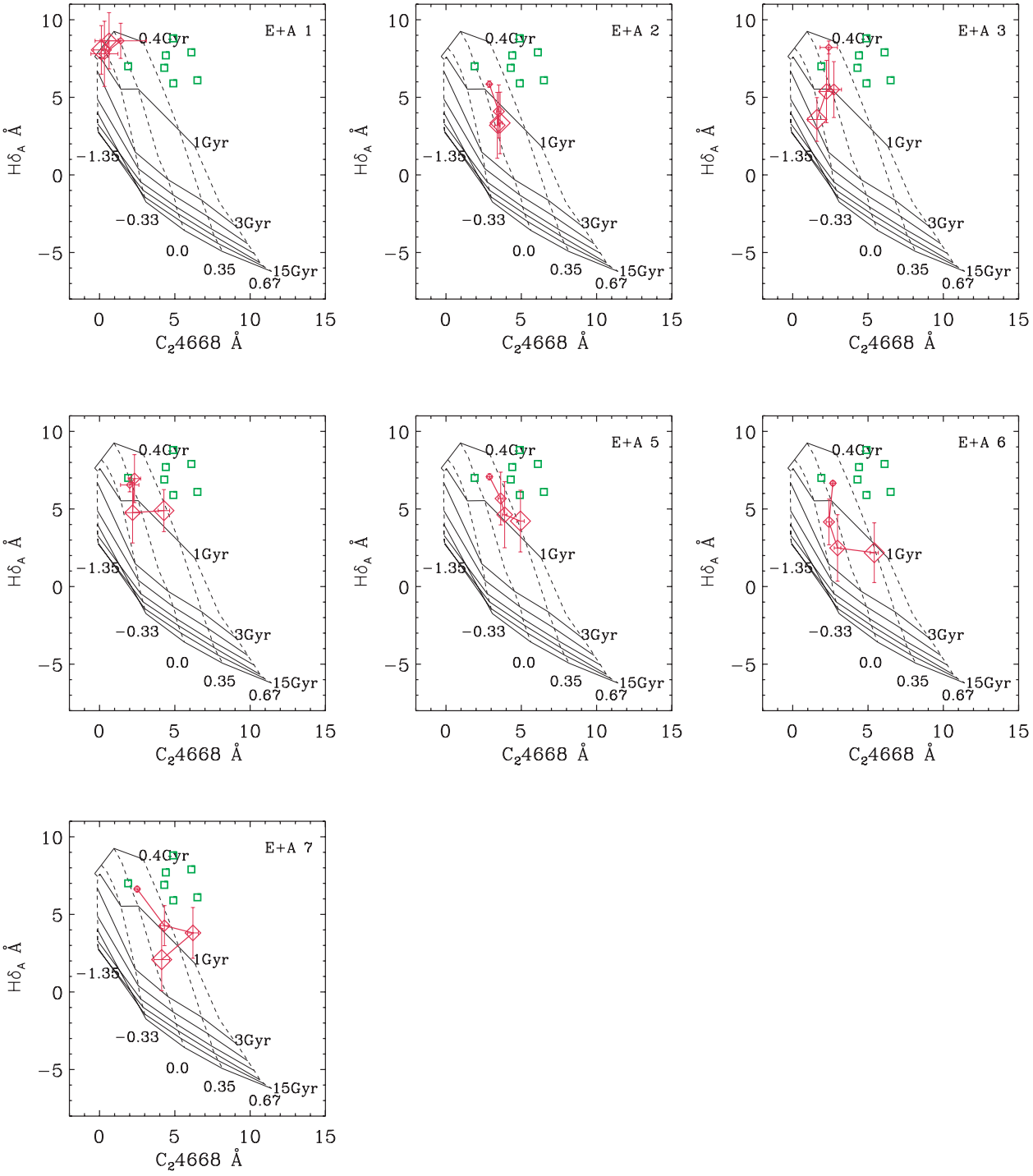

Figure 4. Age–metallicity diagnostic diagrams using the Hδ and $C_2$4668 lines. The radial annular EW measurements are displayed as *red diamonds* with symbol sizes increasing with galactocentric radius. The *green squares* are the global values from the Pracy et al. (2009) sample.

In Fig. 6 we show spatially resolved emission line maps for the [N II] and Hα lines in columns 1 and 2, respectively. The three galaxies that show Hα in emission in the integrated SDSS spectra, (E+A 2, E+A 3 and E+A 5) in Fig. 2, have their emission confined to the central region. In the case of E+A 3, there is convincing emission in only a single spaxel in the galaxy centre and most of the galaxy has Hα in absorption. The rest of the sample shows no evidence for emission at larger galactic-centric radii that would not have been contained in the 3-arcsec SDSS aperture. The weak values of Hα emission in E+A 1 are essentially due to noise, and inspection of the spectra (which are poor quality for this galaxy) shows little evidence for emission or absorption.

In column 3 of Fig. 6, we attempt to correct for the issue of stellar absorption on the Hα emission-line index measurements. This is done by measuring the Hα line EW from the spectrum of the best-fitting stellar population model to the blue arm data. This gives an estimate of the strength of the underlying Hα absorption due to integrated light from the stellar atmospheres alone. This can then

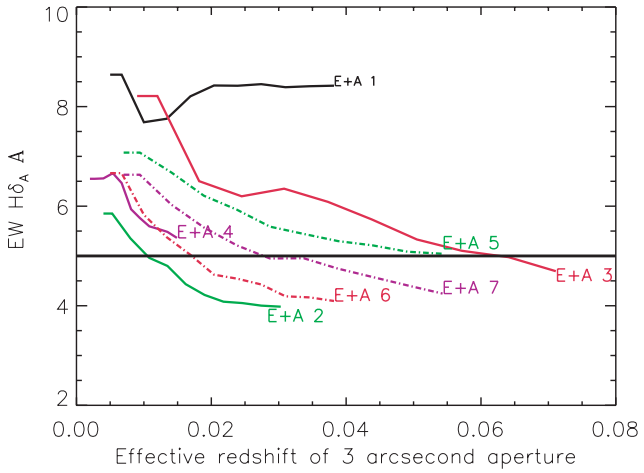

Figure 5. The effect of changing the redshift each galaxy is observed at on the Hδ EW measured by an SDSS fibre. We plot Hδ EW measured in different apertures versus the redshift that galaxy would be at to make the 3-arcsec aperture – the diameter of the SDSS fibres.

be subtracted from the observed line EW to obtain an estimate of EW of the emission. Maps with this correction to the Hα emission are shown in column 3 of Fig. 6. The central Hα emission is still clear in E+A 2, E+A 3 and E+A 5 with stronger absolute EWs. In addition, E+A 4 and E+A 6 also show a weak enhancement of emission in the galaxy centre and E+A 7 shows greater emission in the galaxy outskirts. E+A 1 has uniform emission after correction of $\sim$5 Å, which is the result of the observed spectra showing little emission or absorption at Hα, but strong absorption in the bluer Balmer lines causing a large correction. The outer regions of the rest of the sample show $\sim$1–2 Å of emission-line filling, indicating there may be small amounts of ongoing star formation or that the fit to the higher order Balmer lines is slightly overestimating the Hα EW.

In the final column of Fig. 6 we plot the ratio of [N II] λ6583/Hα λ6563 where we have used the corrected Hα value. We only plot spaxels which have EW(Hα) and EW([N II] λ6583) $>$ 0.2 Å and a S/N in both these lines greater than 2. The most common diagnostic plot for classifying emission line galaxies is the BPT diagram (Baldwin et al. 1981) and uses the position of a galaxy in the two dimensional [O III]/Hβ versus [N II]/Hα plane. However, this diagnostic cannot be used for many weak line galaxies or low S/N spectra where the Hβ and/or [O III] lines cannot be satisfactorily measured – which is the case here. For this reason, Cid Fernandes et al. (2011) developed several more inclusive diagnostics for emission-line taxonomy, the simplest of which uses the EW(Hα) versus [N II]/Hα plane, which is available here. Optimal transpositions of the common division lines for classifying objects as star forming, Seyfert or LINER in the traditional BPT diagram (Kewley et al. 2001, 2006; Kauffmann et al. 2003; Stasińska et al. 2006) are derived by Cid Fernandes et al. (2011). In this plane the standard division between star formation and AGN of Kauffmann et al. (2003) translates to [N II] λ6583/Hα λ6563 $\sim$ 0.5 with values lower than this being in the star formation regime. The hard upper limit for star-forming galaxies of Kewley et al. (2001) translates to [N II] λ6583/Hα λ6563 $\sim$ 0.8 with galaxies between these two values being composite systems and galaxies above the Kewley et al. (2001) value being pure AGN (Cid Fernandes et al. 2011). Comparing these values with the maps in the final column of Fig. 6 for the galaxies with Hα emission shows E+A 2 and E+A 5 have [N II] λ6583/Hα λ6563 $\sim$ 0.5–0.7 corresponding to the transition region whilst E+A 3, the only late-type disc system in the sample, has a line ratio consistent with pure star formation. A bright point-like continuum source was detected in the centre of E+A 5 in the FIRST survey (Becker, White & Helfand 1995) consistent with the presence of an AGN in this galaxy.

Since our spectra extend bluewards of the [O II] λ3727 line we can check whether the three galaxies with Hα emission would have been selected in the sample if the [O II] λ3727 line was available and the normal [O II] $\lambda3727 > -2.5$ Å selection cut was applied. We measured the [O II] λ3727 line EW in a 3-arcsec aperture centred on the galaxy to match the SDSS fibre size. The [O II] λ3727 EW of E+A 2 is $\sim -1.9 \pm 0.7$ Å satisfying the normal selection criterion. E+A 3 and E+A 5 have [O II] λ3727 EWs of $\sim -2.7 \pm 2.3$ and -5.2 ± 1.3 Å, respectively, both slightly above the threshold, although in the case of E+A 2 it is well within the error. The rest of the sample have [O II] $\lambda3727 > -2.5$ Å and consistent with zero at 1σ.

4.5 Kinematics

Two-dimensional streaming velocity maps are shown in Fig. 7 and all the galaxies except E+A 1 and E+A 3 show rotation at some level. In the case of E+A 3, this is surprising since it is a disc galaxy viewed somewhat edge-on and rotation is to be expected. E+A 3 is the faintest and highest redshift galaxy in our sample and was observed in very poor seeing and it maybe the case that the data quality is insufficient to detect the velocity field. Using a parameter, λ_R, derived from two-dimensional spectroscopy, early-type galaxies can be separated into two distinct kinematic categories: fast and slow rotators (Emsellem et al. 2007). The λ_R parameter involves a luminosity-weighted average over the kinematic field obtained from IFU spectroscopy. Emsellem et al. (2007, 2011) found that approximately three quarters of the SAURON sample were fast rotators. Likewise, in a sample of eight E+A galaxies selected from the 2dFGRS and followed up with integral field spectroscopy, seven were found to be fast rotators (Pracy et al. 2009). The prevalence within the E+A population of fast rotators argues that unequal mass mergers rather than major mergers were the dominant progenitors to the E+A galaxies since the probability of rotating remnants increases with increasing merger mass ratio (Bournaud et al. 2008). Although major mergers can still produce fast-rotating remnants (Bois et al. 2011).

In Fig. 8 we plot the values of λ_R for the early-type galaxies in our sample (not including E+A 1 and E+A 3, which are irregular and late-type disc systems) versus the radius over which it is measured (top panel) and against ellipticity at one effective radius (bottom panel). The streaming velocities and velocity dispersions used to calculate λ_R were derived from the spectral fitting described in Section 3.4. We overlay in Fig. 8 the data from the SAURON sample for fast rotators (blue lines and symbols) and slow rotators (red lines and symbols). In all five cases, our data overlap the fast-rotator regions of these plots consistent with previous findings (Pracy et al. 2009). The λ_R values for NGC 3156 (E+A 2) from the SAURON sample are shown as a thick line and large filled diamond in the top and bottom panels, respectively. These can be directly compared with the value for E+A 2 from our measurements; the derived values of λ_R are similar with the SAURON study value $\sim$0.1 larger.

There is a minimum accurately measurable value for λ_R (Emsellem et al. 2007) which depends on the quality of the data. Since λ_R depends on the square of the velocity of each spaxel, even for data with zero true rotation, random noise will induce a non-zero positive value of λ_R. To determine if our derived values of λ_R are

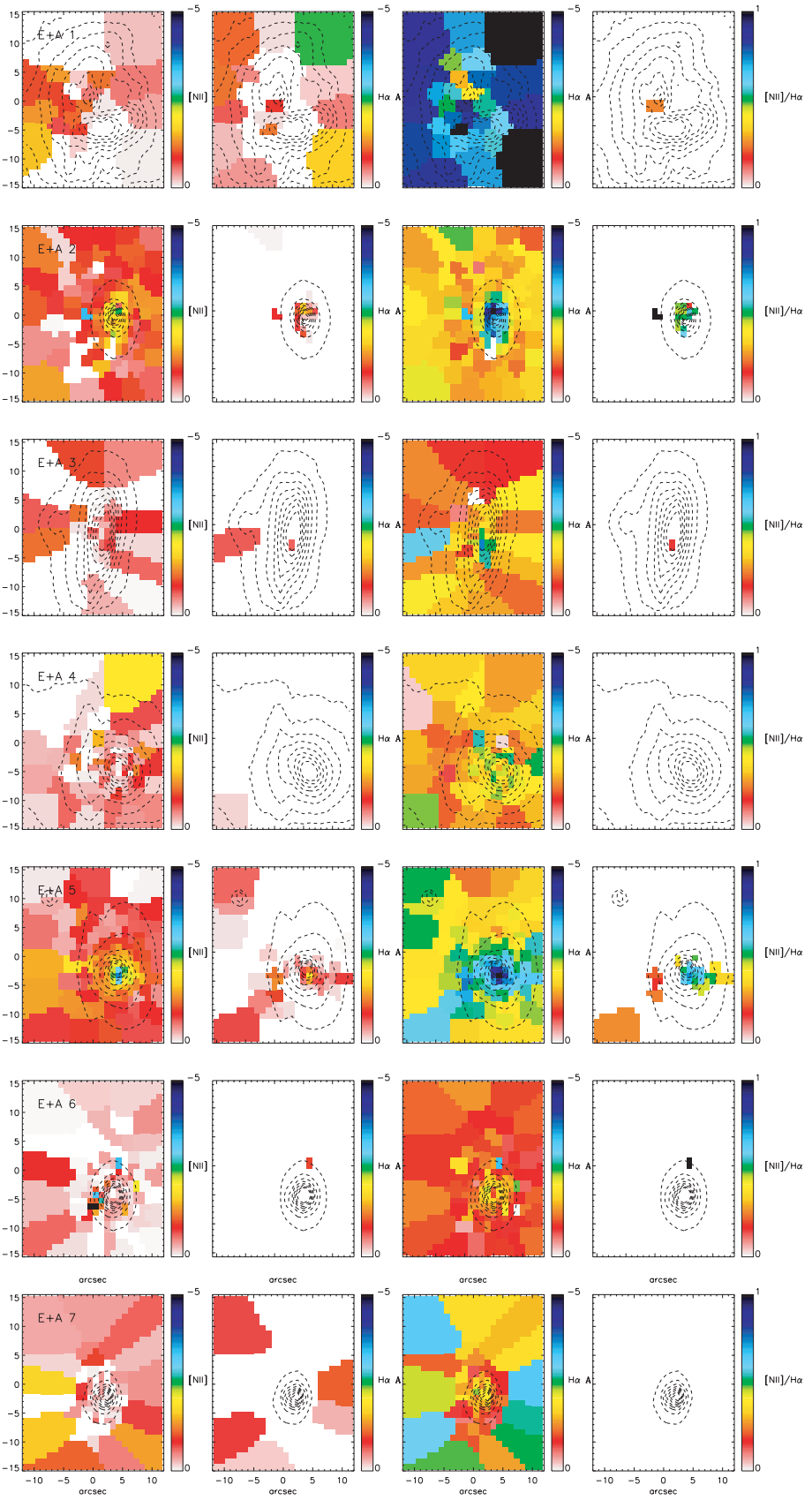

Figure 6. Emission line strength and diagnostic maps. The first column is the [N II] λ6583 EW map; the second column is the Hα emission EW map; the third column is the Hα EW map after correction for underlying stellar absorption; and the final column shows the [N II] λ6583/Hα ratio (corrected) which can be used to classify the source of the ionizing radiation. The contours overlaid are the galaxy integrated light isophotes.

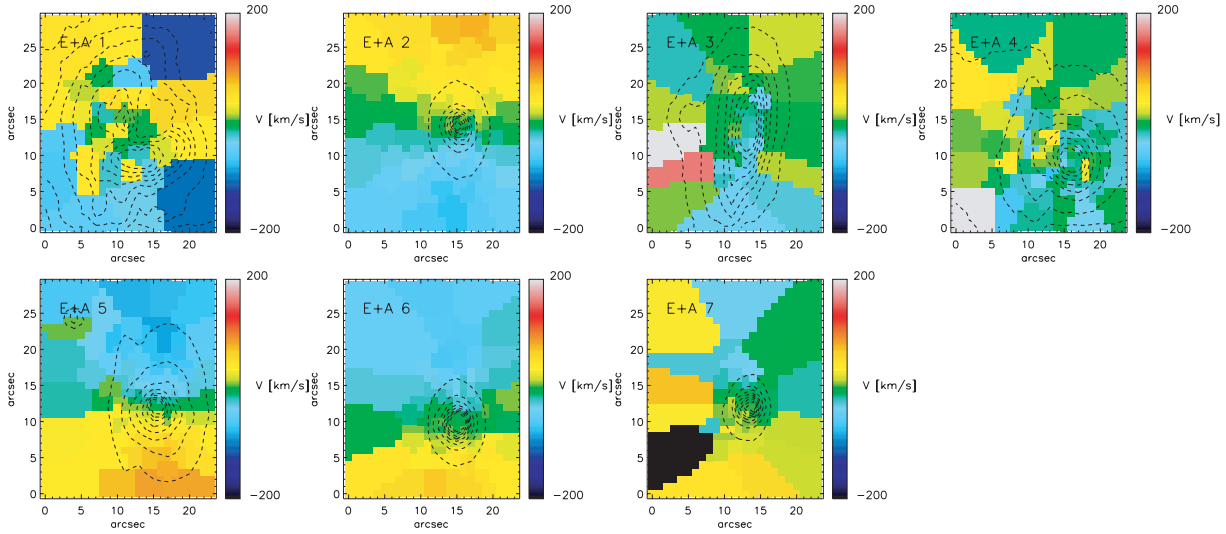

Figure 7. The stellar streaming velocity maps for our sample. E+A 1 and E+A 3 have no detectable rotation and E+A 4 has only marginal evidence for rotation. The remaining galaxies all show clear rotation fields. The black contours overlaid are the galaxy integrated light profiles.

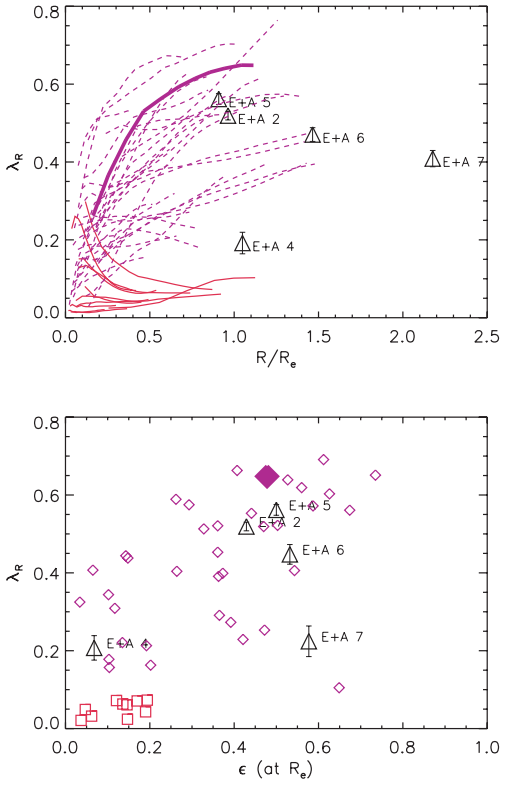

Figure 8. Top panel: the λ_R parameter versus the radius over which it was measured for the early-type galaxies in our sample. We measured λ_R over a circular aperture which is 85 per cent covered by the IFU data and correct the radius to an effective circular radius which has the same areal coverage. The tracks for λ_R from the SAURON sample (Emsellem et al. 2007) are overlaid as blue dashed lines for the fast rotators and as red solid lines for the slow rotators. Bottom panel: the λ_R parameter versus ellipticity measured at one effective radius. Again the SAURON data are overlaid for fast (blue diamonds) and slow (red squares) rotators. The SAURON data for NGC 3156 (E+A 2) are plotted as a thick line (top panel) and filled large diamond (bottom panel).

reliable we simulate this effect by setting the velocity values in each spaxel to zero and adding a random velocity drawn from a normal distribution with a width determined by the velocity error for that spaxel. We use 10 000 such simulations for each galaxy to estimate the minimum value of λ_R that can be reliably measured. For E+A 2 and E+A 5, this value is $\lesssim$15 per cent of the measured value and these galaxies can be confidently classified as fast rotators. For E+A 7 this value is $\sim$40 per cent, and in the cases of E+A 4 and E+A 6 the minimum measurable values are of order 60 per cent of the measured values. In a similar way we calculated the errors on the λ_R values by randomly varying the streaming velocity and velocity dispersion of each spaxel and using the scatter in the resulting values of λ_R as an estimate of the error.

5 DISCUSSION

By selecting a sample of E+A galaxies that are considerably closer, but less massive, than previously studied systems, we have been able to obtain spatially resolved spectroscopy of the core (1 kpc) region of E+A galaxies for the first time. Models that form E+A galaxies through tidal interactions or mergers suggest that starbursts occur in the core of the galaxies due to tidal torques funnelling gas into the core (Mihos & Hernquist 1994; Barnes & Hernquist 1996; Hopkins et al. 2009; Snyder et al. 2011). This region should be compact, on scales of $\sim$1 kpc (Barnes & Hernquist 1996; Bekki et al. 2005; Hopkins et al. 2009) and contain strong stellar population gradients observable as Balmer line gradients (Bekki et al. 2005; Pracy et al. 2005; Snyder et al. 2011). The primary motivation of our observations was to test these predictions by acquiring spatially resolved spectroscopy that resolved this region.

Previous studies, which used colours from imaging (Yang et al. 2008) or spectroscopy that does not resolve the core (Norton et al. 2001; Chilingarian et al. 2009), have suggested that the post-starburst region is centrally concentrated but not necessarily confined to the galaxy core. Other groups have been unable to detect any evidence for a central concentration in their observations (Yagi & Goto 2006; Pracy et al. 2009). The most distant object in our sample has a redshift of $z \sim 0.009$ corresponding to a physical to angular

scale of $\sim$0.18 kpc arcsec^{-1} which allowed us (for this worst case object) to easily spatially resolve the central 1-kpc region even in moderate seeing conditions. The resulting Balmer line EW maps confirm that the post-starburst region is centrally concentrated and contained within $\lesssim$1 kpc (see third column of Fig. 3) consistent with model expectations. The radial profiles of the Balmer line absorption maps which reveal a steep negative Balmer line gradient are consistent with the model predictions for E+A galaxies produced from mergers or tidal interactions (Pracy et al. 2005). The exception is E+A 1 which has uniformly strong Balmer line absorption and no radial gradient. E+A 1 differs from the rest of the sample in other respects: it is the only galaxy with an irregular morphology; it is the bluest galaxy in the sample by a considerable margin and has the strongest Balmer line EW values implying a younger post-starburst age. After emission line filling is taken into account, it has stronger residual Hα emission than the rest of the sample indicating more ongoing star formation which is distributed over the entire galaxy. E+A 1 may represent an earlier evolutionary stage than the other galaxies in the sample or a different class of object altogether.

It has been pointed out by Snyder et al. (2011) that the presence of strong radial Balmer gradients in E+A galaxies means that the galaxies selected by a given EW criterion depend on the galaxy distance, since a fixed diameter fibre will subtend a greater physical distance at higher redshift. For centrally concentrated Balmer gradients, this implies that for a given selection criterion a more extreme population will be selected at higher redshift. This is due to the aperture at higher redshifts including more light from larger galactocentric radii where the Balmer line absorption is weaker. At the median redshift of our sample, the 3-arcsec fibre of the SDSS subtends just $\sim$300 pc, whereas at the median redshift of the SDSS ($z \sim 0.1$) a 3-arcsec fibre subtends $\sim$5 kpc. For our galaxies, the strong radial gradients and strong 'E+A levels' of Balmer line absorption are contained within the central few hundred parsecs. Similar galaxies at higher redshift would not necessarily be classified as E+A galaxies. Selecting galaxies based on measurements from a central fibre also biases us against selecting galaxies which have positive Hδ gradients (central deficits) which are expected from the sudden truncation of star formation in a disc (Pracy et al. 2005). Our sample contains on average less luminous galaxies and also objects with less extreme overall absorption line strengths than many of the previous E+A samples in the literature.

The morphologies of the galaxies in our sample, like E+A samples in general, are mostly early types with the exceptions being one late-type irregular galaxy and one late-type disc galaxy. Most of the early-type galaxies are isolated systems with no interacting neighbour present – see Table 1 for a list of morphologies and environments for the sample. This isolation rules out ongoing interactions as the cause of the post-starburst signature and argues in favour of these galaxies being merger remnants where the progenitors have already coalesced and relaxed. The kinematics of the early types in our sample are all consistent with being fast rotators as defined by Emsellem et al. (2007). This suggests that the mergers producing the E+A galaxy are often unequal mass or minor mergers, since mergers with mass ratios around unity will more commonly result in a non-rotating remnant (Bournaud et al. 2008), although this does not strictly rule out major mergers (Bois et al. 2011). This same conclusion was reached by Pracy et al. (2009) for E+A galaxies selected from the 2dFGRS and is in agreement with the recent findings of Crockett et al. (2011). The two late-type galaxies in our sample (E+A 1 and E+A 3) both have near neighbours which are very close in the case of E+A 1 ($\sim$5 kpc) or much more massive in the case of E+A 3 (see Table 1, for details) and for these two galaxies the E+A signature could be explained by tidal interactions rather than merging.

There are detectable emission lines in two of the early-type galaxies as well as in the late-type disc galaxy. The emission is centrally concentrated and absorption-corrected line ratios imply that in the early-type galaxies this emission is, at least in part, due to AGN activity. The line ratios in the disc galaxy are more consistent with pure star formation. There are other known examples of low-power AGN in E+A galaxies (Liu et al. 2007; Chilingarian et al. 2009) and it has been proposed that nuclear activity, in addition to supernova feedback, contributes to the truncation of star formation in E+A galaxies (Kaviraj et al. 2007). However, simulations have shown that the effect on the post-starburst phase from AGN feedback is weak (Wild et al. 2009; Snyder et al. 2011), with the dominant effect being an increase in the observed post-starburst signature as a result of the expulsion of obscuring dust.

6 CONCLUSIONS

We have selected a new local sample of seven E+A galaxies from the SDSS with a redshift limit of $z = 0.01$ and obtained integral field spectroscopy with the WiFeS instrument on the ANU 2.3-m telescope. The low redshift of our sample allowed for much better physical scale resolution in the core region of the E+A galaxies than previous studies. This allowed us to unequivocally verify that the post-starburst regions are centrally concentrated, consistent with expectations. In summary our main conclusions are as follows.

(i) Six of the seven E+A galaxies and all galaxies with regular morphologies have a centrally concentrated young stellar population and negative Balmer line gradients on scales of $\lesssim$1 kpc. The exception is the only irregular galaxy in the sample which shows uniform Balmer absorption strength and stronger overall absorption compared to the other galaxies.

(ii) The sample is dominated by isolated early-type galaxies. All the early-type galaxies show some level of rotation and are consistent with the fast-rotator population.

(iii) In the early-type galaxies, the combination of a centralized young population and isolation argues in favour of a merger origin where the progenitors have already coalesced.

(iv) The two late-type galaxies in the sample have nearby companions and their spectral signature could be explained by tidal interaction.

ACKNOWLEDGMENTS

We acknowledge the financial support of the Australian Research Council throughout the course of this work. This research has made use of the NASA/IPAC Extragalactic Database (NED) which is operated by the Jet Propulsion Laboratory, California Institute of Technology, under contract with the National Aeronautics and Space Administration. MBP would like to thank the School of Physics at the University of New South Wales for their hospitality. We thank the referee for helpful comments that improved this paper.

REFERENCES

Baldwin J. A., Phillips M. M., Terlevich R., 1981, PASP, 93, 5
Barnes J. E., Hernquist L., 1996, ApJ, 471, 115
Becker R. H., White R. L., Helfand D. J., 1995, ApJ, 450, 559
Bekki K., Shioya Y., Couch W. J., 2001, ApJ, 547, L17
Bekki K., Couch W. J., Shioya Y., Vazdekis A., 2005, MNRAS, 359, 949
Blake C. et al., 2004, MNRAS, 355, 713

Bois M. et al., 2011, MNRAS, 416, 1654
Bothun G. D., Dressler A., 1986, ApJ, 301, 57
Bournaud F., Bois M., Emsellem E., Duc P. A., 2008, Astron. Nachr., 329, 1025
Caldwell N., Rose J. A., Franx M., Leonardi A. J., 1996, AJ, 111, 78
Cappellari M., Copin Y., 2003, MNRAS, 342, 345
Cappellari M., Emsellem E., 2004, PASP, 116, 138
Chilingarian I. V., De Rijcke S., Buyle P., 2009, ApJ, 697, L111
Cid Fernandes R., Stasińska G., Mateus A., Vale Asari N., 2011, MNRAS, 413, 1687
Couch W. J., Sharples R. M., 1987, MNRAS, 229, 423
Crockett R. M. et al., 2011, ApJ, 727, 115
de Zeeuw P. T. et al., 2002, MNRAS, 329, 513
Dopita M., Hart J., McGregor P., Oates P., Bloxham G., Jones D., 2007, Ap&SS, 310, 255
Dopita M. et al., 2010, Ap&SS, 327, 245
Dressler A., Gunn J. E., 1983, ApJ, 270, 7
Emsellem E. et al., 2007, MNRAS, 379, 401
Emsellem E. et al., 2011, MNRAS, 414, 888
Goto T., 2005, MNRAS, 357, 937
Goto T., 2007, MNRAS, 381, 187
Gunn J. E., Gott J. R. I., 1972, ApJ, 176, 1
Hernquist L., 1992, ApJ, 400, 460
Hibbard J. E., Yun M. S., 1999, ApJ, 522, L93
Hopkins P. F., Cox T. J., Younger J. D., Hernquist L., 2009a, ApJ, 691, 1168
Hopkins P. F., Cox T. J., Dutta S. N., Hernquist L., Kormendy J., Lauer T. R., 2009b, ApJS, 181, 135
Kauffmann G. et al., 2003, MNRAS, 346, 1055
Kaviraj S., Kirkby L. A., Silk J., Sarzi M., 2007, MNRAS, 382, 960
Kewley L. J., Dopita M. A., Sutherland R. S., Heisler C. A., Trevena J., 2001, ApJ, 556, 121
Kewley L. J., Groves B., Kauffmann G., Heckman T., 2006, MNRAS, 372, 961
Kohno K., Tosaki T., Matsushita S., Vila-Vilaó B., Shibatsuka T., Kawabe R., 2002, PASJ, 54, 541
Kuntschner H. et al., 2010, MNRAS, 408, 97
Liu C. T., Hooper E. J., O'Neil K., Thompson D., Wolf M., Lisker T., 2007, ApJ, 658, 249
Mihos J. C., Hernquist L., 1994, ApJ, 437, L47
Mihos J. C., Hernquist L., 1996, ApJ, 464, 641
Moore B., Lake G., Katz N., 1998, ApJ, 495, 139
Norton S. A., Gebhardt K., Zabludoff A. I., Zaritsky D., 2001, ApJ, 557, 150
Poggianti B. M., Smail I., Dressler A., Couch W. J., Barger A. J., Butcher H., Ellis R. S., Oemler A. J., 1999, ApJ, 518, 576
Pracy M. B., Couch W. J., Blake C., Bekki K., Harrison C., Colless M., Kuntschner H., de Propris R., 2005, MNRAS, 359, 1421
Pracy M. B., Kuntschner H., Couch W. J., Blake C., Bekki K., Briggs F., 2009, MNRAS, 396, 1349
Pracy M. B., Couch W. J., Kuntschner H., 2010, Publ. Astron. Soc. Australia, 27, 360
Rothberg B., Joseph R. D., 2004, AJ, 128, 2098
Sánchez-Blázquez P. et al., 2006, MNRAS, 371, 703
Shioya Y., Bekki K., Couch W. J., 2004, ApJ, 601, 654
Snyder G. F., Cox T. J., Hayward C. C., Hernquist L., Jonsson P., 2011, ApJ, 741, 77
Springel V., Hernquist L., 2003, MNRAS, 339, 289
Springel V., Di Matteo T., Hernquist L., 2005, MNRAS, 361, 776
Stasińska G., Cid Fernandes R., Mateus A., Sodré L., Asari N. V., 2006, MNRAS, 371, 972
Thomas D., Maraston C., Bender R., 2003, MNRAS, 339, 897
Thomas D., Maraston C., Korn A., 2004, MNRAS, 351, L19
Trager S. C., Worthey G., Faber S. M., Burstein D., Gonzalez J. J., 1998, ApJS, 116, 1
Vazdekis A. et al., 2007, in Vazdekis A., Peletier R. F., eds, Proc. IAU Symp. 241, Stellar Population SEDs. Cambridge Univ. Press, Cambridge, p. 133
Veilleux S., Osterbrock D. E., 1987, ApJS, 63, 295
Wild V., Walcher C. J., Johansson P. H., Tresse L., Charlot S., Pollo A., Le Fèvre O., de Ravel L., 2009, MNRAS, 395, 144
Worthey G., Ottaviani D. L., 1997, ApJS, 111, 377
Yagi M., Goto T., 2006, AJ, 131, 2050
Yang Y., Zabludoff A. I., Zaritsky D., Mihos J. C., 2008, ApJ, 688, 945
Zabludoff A. I., Zaritsky D., Lin H., Tucker D., Hashimoto Y., Shectman S. A., Oemler A., Kirshner R. P., 1996, ApJ, 466, 104

This paper has been typeset from a TEX/LATEX file prepared by the author.